GDCh Research Article Angewandte International Edition Chemie www.angewandte.org

How to cite: *Angew. Chem. Int. Ed.* **2025**, e202508426
doi.org/10.1002/anie.202508426

Graphene Nanoribbons

Chirality Unbound in Graphene Nanoribbons

Si Tong Bao[+], Yongseok Hong, Haoyu Jiang, Luke T. Lackovic, Shayan Louie, Ding Xu, Fay Ng, Nicholas Olsen, Xiaoyang Zhu, Michael L. Steigerwald, Milan Delor, Colin Nuckolls,* and Qifeng Jiang[+]**

Abstract: In this manuscript, we report the first demonstration of controlled helicity in extended graphene nanoribbons (GNRs). We present a wealth of new graphene nanoribbons that are a direct consequence of the high-yielding and robust synthetic method revealed in this study. We created a series of defect-free, ultralong, chiral cove-edged graphene nanoribbons where helical twisting of the graphene nanoribbon backbone is tuned through functionalization with chiral side chains. *S*-configured point chiral centers in the side chains transfer their chiral information to induce a helically chiral, right-handed twist in the graphene nanoribbon. As the backbone is extended, these helically twisted graphene nanoribbons exhibit a substantial increase in their circular dichroic response. The longest variant synthesized consists of an average of 268 linearly fused rings, reaching 65 nm in average length with nearly 10 full end-to-end helical rotations. The structure exhibits an extraordinary $|\Delta\varepsilon|$ value of 6780 M^{-1} cm^{-1} at 550 nm—the highest recorded for an organic molecule in the visible wavelength range. This new chiroptic material acts as room-temperature spin filters in thin films due to its chirality-induced spin selectivity.

Introduction

This manuscript describes new graphene nanoribbons (GNRs) where the direction of their helical twist can be controlled over the entire length of the ribbon, creating materials that act as spin filters in thin films. As an emerging class of next-generation electronic materials, GNRs exhibit a variety of fascinating optoelectronic properties that can be tailored through tuning their edge structure, topology, and length, as well as through chemical functionalization. Cove-edged GNRs (Figure 1a) feature a nonplanar geometry resulting from [4]helicene subunits on the edges. In principle, these cove-edged GNRs are capable of exhibiting chiroptical properties with a preference for *P* or *M* helicity of the ribbons. Despite the wealth of surface[1–8] and solution-based[9–17] synthetic approaches, crafting extended cove-edged GNRs with a helical twist of defined handedness remains a significant challenge. Even more broadly, controlling the twisting in ladder polymers, in general, is an unmet challenge. For cove-edged GNRs (Figure 1a), the difficulty in controlling the helical twisting is due in part to the rapid interconversion between different conformations of the [4]helicene subunits.[18] In addition, a defect-free graphitized backbone is essential, as any freely rotating bonds (referred to as defects) will interrupt the helical twist. Achieving chiral cove-edged ribbons of a single handedness will enable exploration of their chiroptic properties and create potential for applications in nonlinear optics,[19] magnetochirality,[20] asymmetric catalysis,[21] and chiral-induced spin selectivity (CISS).[22–24]

The chiral GNR oligomers are designated as ***c*hGNR[*n*]**, where *n* represents the exact number of PDI units, and the chiral GNR polymers are designated as ***c*hGNR[~*n*]**, where ~*n* represents the average number of perylene diimide (PDI) units in the polymer (Figure 1b). We recently found that chiral substituents on PDI dimers, the shortest oligomer ***c*hGNR[2]** can induce helicity in the aromatic core.[25,26] To illustrate the complexity of the stereoinduction in these oligomers/polymers, Figure 1c displays a trimeric subunit of ***c*hGNR**s which can fluctuate among three conformations: the helical chiral conformer, the waggling achiral (*meso*) conformer, and the helical conformer of the opposite chirality. This complexity increases as the oligomers grow longer, making helicity control more challenging and potentially diminishing the chiroptical response due to the complicated distribution of multiple conformers. We report here two new synthetic methods that enable remarkably high helicity control in two sets of ***c*hGNR**s: one type comprises atomically defined oligomers up to 10 PDIs in length to understand and benchmark chiral information transfer; the other type are polymers whose length can be controlled by the incorporation of capping subunits in the polymerization. While there are numerous examples of conjugated polymers with rotatable single bonds that can be wound into helical structures,[27–30] there are no means to control the direction of twisting in graphene nanoribbons or even more broadly in ladder polymers. Controlling helicity

[*] S. T. Bao[+], Y. Hong, H. Jiang, L. T. Lackovic, S. Louie, D. Xu, F. Ng, N. Olsen, Prof. X. Zhu, M. L. Steigerwald, Prof. M. Delor, Prof. C. Nuckolls, Dr. Q. Jiang[+]
Department of Chemistry, Columbia University, New York, New York 10027, USA
E-mail: milan.delor@columbia.edu
cn37@columbia.edu
qj2175@columbia.edu

[+] Both authors contributed equally to this work.

Additional supporting information can be found online in the Supporting Information section

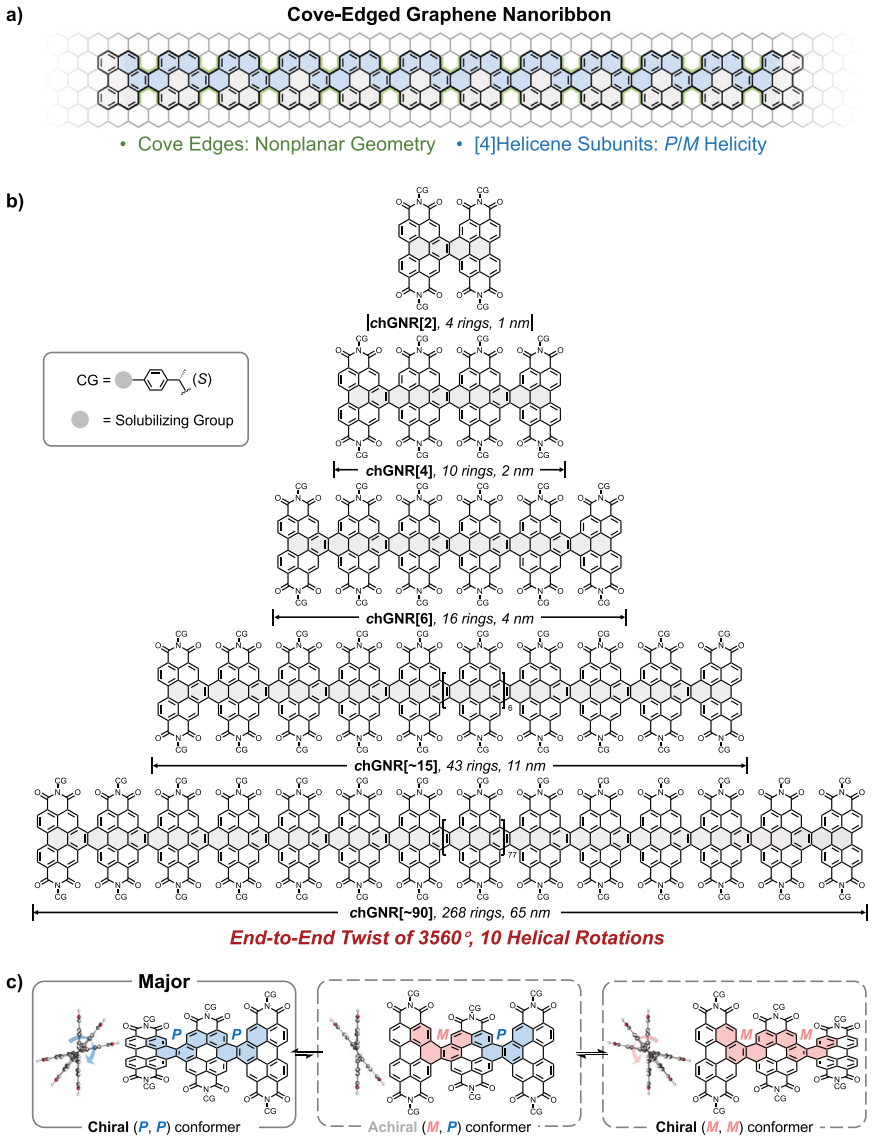

Figure 1. Chiral helical graphene nanoribbons (***ch*GNRs**). a) Cove-edged graphene nanoribbon cut from a graphene sheet. b) Structures of ***ch*GNRs**. c) Dynamic helicity in ***ch*GNRs** demonstrated by the trimer (*S*)-**chGNR[3]** wherein the chiral (*P*, *P*) conformer is predominant.

in GNRs provides access to an untapped vein of new materials.

The materials described here provide the first example of helicity control in chiral cove-edged GNRs (Figure 1a). The longest polymer ***ch*GNR[~90]** contains on average 90 PDI units and 268 fused rings, spanning 65 nm in length. We find that chiral side chains in ***ch*GNRs** enforce a helical winding in the GNR backbone and exhibit a strong chiroptical response in circular dichroism (CD) spectroscopy. As the backbones elongate, there is an increase in the CD response at ~550 nm and the maximum absorption wavelength. The longest polymer, ***ch*GNR[~90]** (Figure 1b), boasts an extraordinary $|\Delta\varepsilon|$ value of 6780 M^{-1} cm^{-1} at 550 nm—the highest recorded for an organic molecule in the visible wavelength range. Films of these ***ch*GNRs** are able to effectively filter electron spins at room temperature. Using femtosecond transient reflectance microscopy, we observed spin-selective charge injection from WSe_2 monolayers to ***ch*GNR** thin films as a result of the CISS effect. While we recently reported spin filtering with surface-active dimers,[31] this is the first example of the CISS effect in an extended GNR system.

Results and Discussion

Synthesis of Defect-Free Nanoribbon Backbones

The helical perylene tetraester ribbons (**hPTR**s) methodology, we developed for the synthesis of ***ch*GNRs**, is shown in Figure 2. While we have reported the synthesis of short oligomers with alkyl side chains through PDI-alkene intermediates,[9,13] it is very challenging to access longer backbones because the iterative synthesis is limited in scalability and cannot be transferred in polymer synthesis. Besides,

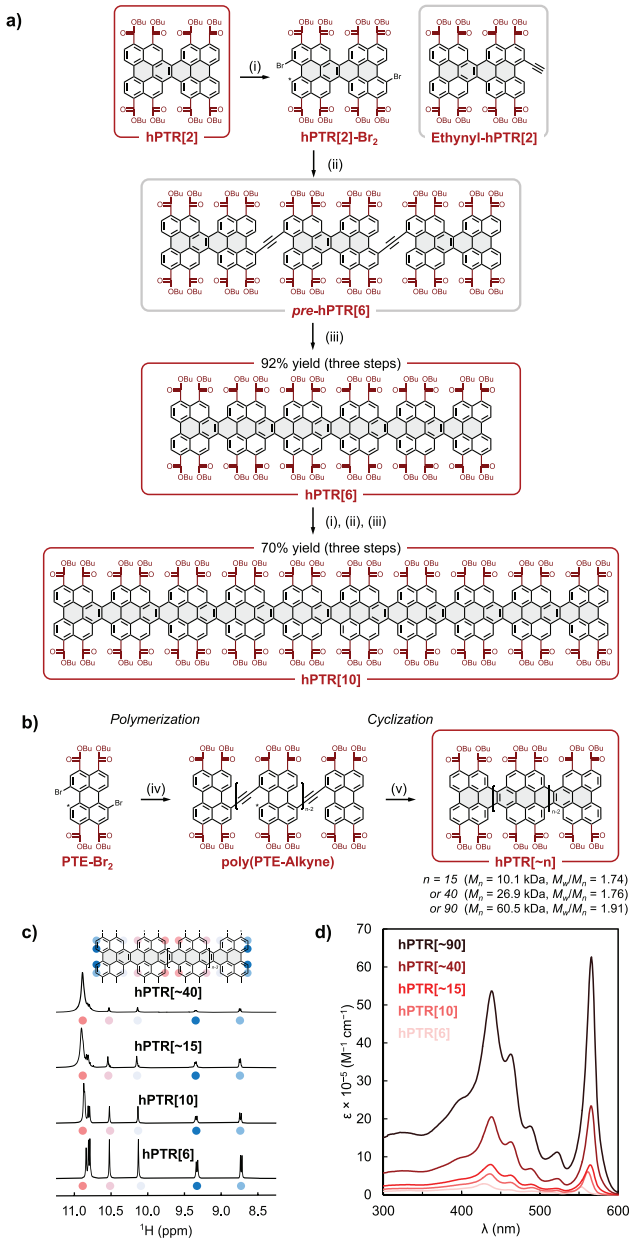

Figure 2. Synthesis of helical perylene tetraester ribbons (**hPTR**s). a) Synthesis of oligomeric **hPTR[10]**. Synthesis of the full library of oligomeric **hPTR**s is shown in Figure S1. i) Br_2, propylene oxide, DCM, room temperature, 2 h; ii) **Ethynyl-hPTR[2]**, $Pd(PPh_3)_2Cl_2$, CuI, THF/Et_3N, 60 °C, 16 h; iii) I_2, hν, PhCl, 72 h. b) Extending **hPTR**s through the polymerization-cyclization strategy. iv) bis(tributylstannyl)acetylene, **PTE-Br**, Pd-P(*t*-Bu)$_3$-G4, K_3PO_4, in toluene, room temperature, 24 h. **PTE-Br** loading: 20 mol% ($n = 15$), 10 mol% ($n = 40$), or 5 mol% ($n = 90$). v) I_2 in PhCl, hν, 72 h. c) Down-field window of the ^{1}H NMR spectra recorded in $CDCl_3$. d) Stacked UV–vis spectra of selected **hPTR**s in $CHCl_3$. Figure S4 shows the full UV–vis spectra for all **hPTR**s.

in these syntheses, the functionality on the imide groups is predetermined by starting PDI building blocks, usually limited to hydrocarbons. The key insight that enabled the synthesis of the oligomers and polymers in this study was exchanging of the PDI subunits, used previously, with the perylene tetraester (PTE) subunits. This seemingly minor modification significantly enhances the structural fidelity along the ladder backbone, allowing the synthesis of longer, defect-free oligomers and polymers, while accommodating a diverse range of substituents along the edges.

Figure 2a displays the synthesis of **hPTR[10]** as an example of the atomically defined oligomers, **hPTR**s (the detailed synthesis of oligomeric **hPTR**s is described in the Figure S1 and Supporting Information). The synthetic sequence consists of bromination, Sonogashira coupling with ethynyl-substituted, dimeric PTE building blocks, and finally an iodine-mediated photocyclization, which is initiated by white light emitting diodes (LEDs). This three-step synthetic route allows us to grow the **hPTR**s by four units per reaction cycle in very high yields (70%–92%). Using this method, we were able to achieve scalable synthesis of **hPTR**s containing 2–10 perylene units in high yields. As a point of emphasis, the outstanding efficiency and high yields of the backbone extension reactions in this new synthetic strategy allow us to make graphene nanoribbons with atomically precise backbones of desired lengths.

We further extend the length of **hPTR**s to polymers using the polymerization-cyclization strategy shown in Figure 2b. The conventional conditions of Stille polycondensation, involving elevated temperatures or microwave irradiation, are known to introduce structural defects arising from homo-coupling side reactions, which hinders subsequent photocyclization and nanoribbon formation.[32] Therefore, our sequence employs a room-temperature Stille polycondensation[33] of dibromo perylene tetraester (**PTE-Br$_2$**) and bis(tributylstannyl)acetylene, facilitating perfectly alternating PTE-alkyne polymer backbones. To maintain the analogous end structures to the atomically precise oligomers, monofunctional **PTE-Br** was added as the end-capping reagent. We then subjected the resulting alternating copolymer **poly(PTE-Alkyne)** to the iodine-mediated photocyclization with white LEDs to form the fully fused **hPTR** ribbons.

The ^{1}H NMR spectra in Figure 2c reveal the length of the ribbons and also their structural integrity (i.e., a fully fused backbone without defects). We find analogous aromatic proton resonances in the polymeric ribbons by comparing them to the shorter ribbons, **hPTR[6]** and **hPTR[10]**, indicating the complete backbone fusion of the polymer precursor. For the polymeric ribbons, we determine their length by end-group analysis using ^{1}H NMR spectra. These analyses indicate the precise control over polymer length, which can be tuned by the amount of the end-capping **PTE-Br**: 15 perylene units with 20 mol% **PTE-Br** (**hPTR[~15]**, M_n = 10.1 kDa), 40 perylene units with 10 mol% **PTE-Br** (**hPTR[~40]**, M_n = 26.9 kDa), and 90 perylene units with 5 mol% **PTE-Br** (**hPTR[~90]**, M_n = 60.5 kDa) on average (Figure S2). The molecular weight distribution (M_w/M_n) of these long polydisperse ribbons was characterized by GPC: 1.74 for **hPTR[~15]**, 1.76 for **hPTR[~40]** and 1.91 for **hPTR[~90]** (Figure S3). The **hPTR**s are soluble in organic chlorinated and aromatic solvents, including chloroform, toluene, and chlorobenzene. As the **hPTR**s increase in length, their absorption spectra and maximum absorption wavelengths

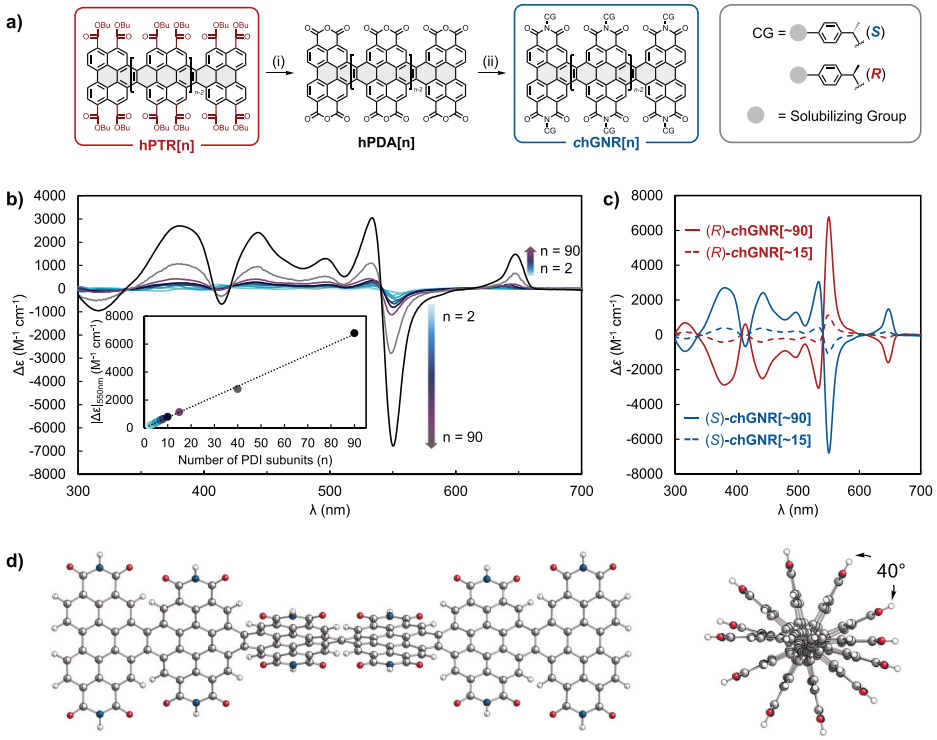

Figure 3. Synthesis and chiroptical properties of ***ch*GNR**s. a) Synthesis of ***ch*GNR**s through post-functionalization of **hPTR**s. i) concentrated H_2SO_4, 60 °C, 16 h; ii) chiral amine, imidazole, 140 °C, 48 h. b) Stacked CD spectra of (*S*)-***ch*GNR**s in TCE at 20 °C. Figures S7–S19 contain the full optoelectronic spectra of all ***ch*GNR**s. c) CD spectra of (*S*)- and (*R*)-***ch*GNR[~15]** and **[~90]** in TCE at 20 °C. d) DFT-optimized geometry of (*S*)-***ch*GNR[6]** (homohelical conformation with pure *P* helicity) at B3LYP-D3/6-31 + G(d) level of theory, showing the torsional angle between neighboring PDI units.

(λ_{max}) undergo bathochromic shifts as the conjugation length increases (Figures 2d and S5).

Helicity Control in Cove-Edged GNR

Figure 3a shows the conversion of both oligomeric and polymeric **hPTR**s into chiral helical graphene nanoribbons (***ch*GNR**s). We first converted the **hPTR**s into their corresponding anhydride (**hPDA[*n*]**) in sulfuric acid, then reacted the anhydride with chiral amines to form the ***ch*GNR** series. We previously found in the dimer, ***ch*GNR[2]**, that the phenylethylamine derivatives were effective in controlling the helicity of the backbone.[25] Modified (*S*)- or (*R*)-phenylethylamines were used to improve the solubility of ***ch*GNR**s (Figure S6). We functionalized the phenyl group with solubilizing side chains containing a chiral center because this sidechain is readily available. This side chain, and its associated racemic chiral center, has no influence on the chiroptical properties of ***ch*GNR**s, as it is spatially distant from the GNR backbone; we verified this by creating and testing derivatives as described in Figure S6. With these chiral side chains, all ***ch*GNR**s are fully soluble in 1,1,2,2-tetrachloroethane (TCE) across a wide range of temperatures.

We observe an enhanced chiroptical response with increasing ribbon length in the CD spectra of (*S*)-***ch*GNR**s (Figure 3b). (*S*)-Phenylethyl point chiral substituent of the imide groups induces *P* helicity to the aromatic core, and the helicity propagates through the ***ch*GNR** backbone. Notably, the $|\Delta\varepsilon|$ of (*S*)-***ch*GNR**s increases with the number of PDI subunits for two separate transitions (Figure 3b). At the maximum absorption wavelength of each (*S*)-***ch*GNR**, we observe an enhancement in $\Delta\varepsilon$. At 648 nm, (*S*)-***ch*GNR[~90]** shows the largest $\Delta\varepsilon$ of 1573 M^{-1} cm^{-1} among all the ***ch*GNR**s. The increase in $\Delta\varepsilon$ and the red-shifted CD signals are consistent with the UV–vis absorption measurements (Figure S20). We also observe increasing $|\Delta\varepsilon|$ of the negative Cotton effect around 550 nm, indicating the presence of a similar but extended helicity compared to the dimer. The longest (*S*)-***ch*GNR[~90]** exhibits an over 38-fold increase in $|\Delta\varepsilon|$ at ~550 nm compared to the shortest (*S*)-***ch*GNR[2]** (6780 M^{-1} cm^{-1} vs. 178 M^{-1} cm^{-1}). The $\Delta\varepsilon$ for ***ch*GNR[~90]** is among the highest reported in the visible range for an organic molecule. The chiral dissymmetry factor $|g_{abs}|$ ($|\Delta\varepsilon|/\varepsilon$) around 550 nm increases linearly with oligomer length: from 2.3×10^{-3} for (*S*)-***ch*GNR[2]** to 4.3×10^{-3} for (*S*)-***ch*GNR[5]**. The value then plateaus and remains near-constant up to (*S*)-***ch*GNR[~90]**. Due to the bathochromic shifting of the optical transitions with length, it is difficult to accurately and meaningfully compare g_{abs} for nanoribbons. Notably, increasing the length or the number of helical twists in the twistacene-based GNRs is known to increase $|\Delta\varepsilon|$, but does not directly affect g_{abs} (Figure S21). Additionally, we find that the direction of ***ch*GNR** helicity can be reversed by changing the chirality of chiral side chains. When the opposite handedness of the chiral amine was used in the functionalization, the resulting

(*R*)-***ch*GNR[~15]** and **[~90]** both exhibit nearly mirrored CD spectra compared to their (*S*)-analogues (Figure 3c). Therefore, the (*R*)-phenylethylamino chiral sidechains induce an *M* helicity in the ***ch*GNR** backbone.

Finally, density functional theory (DFT) calculations reveal the structural property of ***ch*GNR**s and support the persistence of helicity over the entire length of the polymer we infer from the linear increase in the CD spectroscopy. Figure 3d shows the optimized geometry of (*S*)-***ch*GNR[6]**, where *P* helicity is induced consistently across all neighboring perylene units along the backbone. The model predicts a ~40° torsional angle between neighboring PDI units, implying in a 360° end-to-end twist every 10 repeating units. We used time-dependent DFT (TD-DFT) calculations to further examine the chiroptical properties of ***ch*GNR**s. The simulated CD spectra of homohelical ***ch*GNR** conformers (Figure S22) suggest that $|\Delta\varepsilon|$ values increase with nanoribbon length for both $S_0 \rightarrow S_1$ (lowest energy transition) and $S_0 \rightarrow S_2$ (approximately 550 nm) transitions (Figure S23a,b), closely matching experimental observations (Figure 3b). However, this trend is significantly disrupted in heterohelical ***ch*GNR** conformers, where the introduction of a [4]helicene subunit of opposite helicity drastically lowers the $|\Delta\varepsilon|$ value for the $S_0 \rightarrow S_2$ transition (Figure S23c–e). For the waggling form of the ***ch*GNR[3]** (Figure 1c), there is no CD signal because it is achiral. For the longer oligomers, with even a single helical reversal, the calculated CD signals are significantly diminished. These results suggest that the loss of control over the helical twist in ***ch*GNR**s would lead to a plateau in $|\Delta\varepsilon|_{550\,nm}$. In contrast, experimental data show that the $|\Delta\varepsilon|_{550\,nm}$ increases nearly linearly with ribbon length, extending up to nanoribbons with 90 PDI units (Figure 3b). These computational studies underscore the critical role of well-controlled helical twisting, driven by side-chain chirality, in maintaining and enhancing the chiroptical properties of ***ch*GNR**s.

Spin Selectivity in Cove-Edged GNRs

CISS is a quantum phenomenon in which the chirality of molecules or materials imparts spin selectivity to electronic processes such as charge transfer and transport.[34,35] To evaluate whether ***ch*GNR** could act as platforms for CISS, we performed all-optical experiments of spin-selective charge injection in ***ch*GNR** thin films. We prepared a heterostructure by spin-casting (*R*)- and (*S*)-***ch*GNR[~15]** films on the 2D semiconductor WSe_2 prepared by mechanical exfoliation on a sapphire substrate (Figure 4a). WSe_2 monolayers exhibit optical selection rules that permit selective excitation of the K or K' valleys through circularly polarized photoexcitation, which in turn enables generating spin-polarized electron-hole pairs (excitons, Figure 4b).[36] Figure 4c shows the band alignment for the heterostructure, indicating favorable electron transfer from the (spin-polarized) conduction band of WSe_2 to the lowest unoccupied molecular orbital (LUMO) level of ***ch*GNR[~15]**, and ruling out the possibility of direct exciton (energy) transfer. We used femtosecond transient reflectance

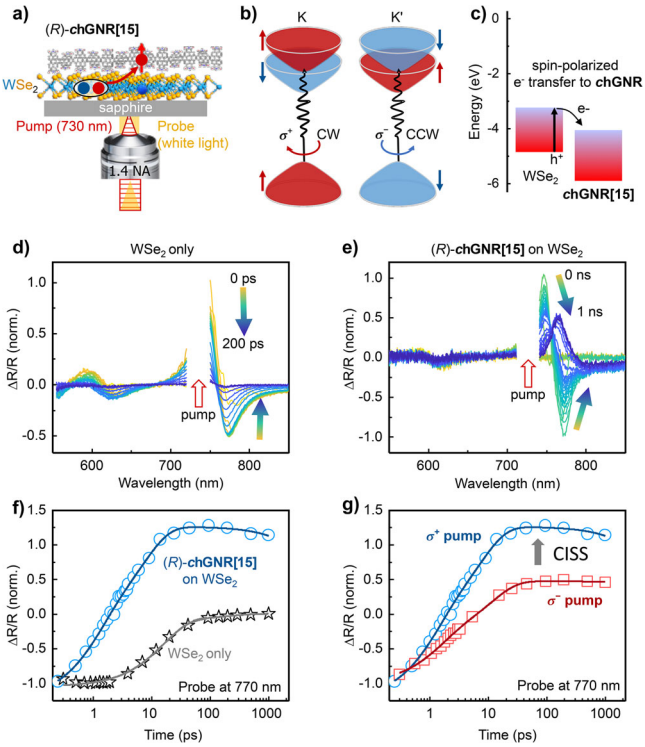

Figure 4. a) Schematic experimental configuration for transient reflectance microscopy on WSe_2/***ch*GNR** heterostructures. b) Spin-valley locking in WSe_2 allows all-optical excitation of spin-polarized excitons. Spin polarization (up or down) is selected through circularly-polarized excitation (clockwise σ^+ or counterclockwise σ^-). c) Band diagram for the WSe_2/***ch*GNR** heterostructure, showing that electron transfer from WSe_2 to ***ch*GNR[~15]** is favored. The HOMO and LUMO energy of (*R*)-***ch*GNR[~15]** is determined by solid-state cyclic voltammetry and UV measurement (Figure S24). d) and e) Transient reflectance spectra as a function of pump-probe time delay following 730 nm pump excitation for WSe_2 only (d) and the WSe_2/(*R*)-***ch*GNR** heterostructure (e). The pump fluence is 12 μJ cm^{-2}. f) Transient reflectance kinetics at a probe wavelength of 770 nm, comparing WSe_2 only and the WSe_2/(*R*)-***ch*GNR[~15]** heterostructure. g) Comparison of transient reflectance kinetics for σ^+ versus σ^- excitation on the WSe_2/(*R*)-***ch*GNR[~15]** heterostructure. σ^+ excitation leads to faster charge injection in (*R*)-***ch*GNR[~15]** and a threefold increase in injection efficiency, suggesting a large CISS effect. All measurements are at room temperature. See data for (*S*)-***ch*GNR[~15]** in Figure S24.

microscopy (Figure 4a, details in Supporting Information) to track photoinduced dynamics in the heterostructure. Importantly, we chose a pump excitation wavelength of 730 nm (1.7 eV), below the lowest optical transition of ***ch*GNR[~15]** and near-resonant with the A-exciton of WSe_2, allowing selective excitation of the WSe_2.

Figure 4d,e display the transient reflectance spectra for a WSe_2 monolayer and the WSe_2/***ch*GNR** heterostructure under identical excitation conditions, and Figure 4f compares the transient kinetics extracted from these spectra at a probe wavelength of 770 nm. In both cases, transient spectra are dominated by the strong photoinduced bleach of the WSe_2 optical transitions. WSe_2 exhibits minimal spectral shifts and complete decay of its excited state within 500 ps. The

WSe_2/***c*hGNR** heterostructure, on the other hand, clearly displays a spectral redshift toward a long-lived (≫1 ns) state. The spectra evolve around a single isosbestic point at 756 nm, suggesting population transfer from one state to another. Based on the band alignment of the heterostructure (Figure 4c), we assign the long-lived state to a charge-transfer state following electron transfer from WSe_2 to ***c*hGNR**. Figure 4g shows that in the WSe_2/(*R*)-***c*hGNR[~15]** heterostructure, σ^+ excitation results in ~1.5-fold larger charge injection kinetics and a ~2.7-fold larger late-time signal compared to σ^- excitation, indicating spin-valley-selective charge injection into (*R*)-***c*hGNR[~15]**. This result is strongly suggestive of a CISS effect in interfacial charge transfer. This large difference between σ^+ and σ^- excitation compares favorably to previous studies of spin-selective charge injection at 2D semiconductor/chiral perovskite interfaces.[37,38] The fastest charge injection rate we observed from σ^+ excitation is $\sim 1\ ps^{-1}$ (Figure 4g), allowing for appreciable charge injection prior to spin depolarization in WSe_2 even at room temperature.[39,40] We observed opposite selectivity of charge injection in the WSe_2/(*S*)-***c*hGNR[~15]** heterostructure, displaying faster charge transfer following σ^- excitation, and a 2.2-fold larger late-time signal compared to σ^+ excitation (Figure S25). These measurements indicate a robust but slightly weaker CISS effect in the (*S*)-***c*hGNR[~15]** enantiomer, possibly due to greater structural heterogeneity in the spin-coated films. Future studies will explore the effect of temperature, heterogeneity, and oligomeric chain length on charge injection kinetics and efficiency. These experiments establish ***c*hGNR** as a promising platform to study CISS, including in all-optical experiments free of complication from metal electrodes.

Conclusion

In conclusion, this work describes the first example of a cove-edged graphene nanoribbons in which the direction of helical twisting can be controlled and their ability to filter electron spins. We put forward two new methods to make nanoribbons of perfect structural integrity across the backbones: unit-to-unit construction with precise length control and a polymerization-functionalization strategy to further extend the ribbons. We synthesized the chiral cove-edged graphene nanoribbons through installation of chiral side chains. These nanoribbons exhibit length-dependent chiroptical properties. In particular, CD of ***c*hGNR[~90]** (maximum $|\Delta\varepsilon|$ of 6780 $M^{-1}\ cm^{-1}$ at 550 nm) is among the largest reported in the visible range for an organic molecule. The effective induction of chirality and length control of defect-free graphene nanoribbons, coupled with their ability to filter spins, highlights their applications in chiral synthesis and spintronics.

Supporting Information

The authors have cited additional references within the Supporting Information.[8,12,41–49]

Acknowledgements

C.N. thanks Sheldon and Dorothea Buckler for their generous support. This research was supported by the National Science Foundation under award number CHE-2304946 and the Defense Advanced Research Projects Agency (DARPA) under agreement no. HR00112390109. Equipment development for transient reflectance microscopy measurements was supported by the National Science Foundation under grant number DMR-2115625. Y.H. acknowledges support from the National Research Foundation of Korea (NRF) grant funded by the Korean government (MSIT) (RS-2023-00240362). The authors thank the Precision Biomolecular Characterization Facility (PBCF) at Columbia University. Essential instrumentation in the PBCF was made possible by funding from the U.S. National Institutes of Health under award number 1S10OD025102-01. NMR spectra reported in this publication were supported by the Office of the Director, the National Institutes of Health, under award number S10OD026749. The content is solely the responsibility of the authors and does not necessarily represent the official views of the National Institutes of Health. The authors thank Dr. John Decatur (Columbia University) for his management of NMR facilities and Dr. Jerry Chang (Columbia University) for his management of PBCF. The authors thank Dr. Daniel Cavlovic (Columbia University), Dr. Scott Docherty (Columbia University), and Prof. Zexin Jin (Westlake University) for their insightful discussion.

Conflict of Interests

The authors declare no conflict of interest.

Data Availability Statement

The data that support the findings of this study are available from the corresponding author upon reasonable request.

Keywords: Chiral-induced spin selectivity · Chirality · Graphene nanoribbons · Ladder polymers

[1] A. Keerthi, C. Sánchez-Sánchez, O. Deniz, P. Ruffieux, D. Schollmeyer, X. Feng, A. Narita, R. Fasel, K. Müllen, *Chem. Asian J.* **2020**, *15*, 3807–3811.
[2] A. Jolly, D. Miao, M. Daigle, J.-F. Morin, *Angew. Chem. Int. Ed.* **2020**, *59*, 4624–4633.
[3] W. Niu, J. Ma, X. Feng, *Acc. Chem. Res.* **2022**, *55*, 3322–3333.
[4] Y. Gu, Z. Qiu, K. Müllen, *J. Am. Chem. Soc.* **2022**, *144*, 11499–11524.
[5] Y. Yano, N. Mitoma, H. Ito, K. Itami, *J. Org. Chem.* **2020**, *85*, 4–33.
[6] R. E. Blackwell, F. Zhao, E. Brooks, J. Zhu, I. Piskun, S. Wang, A. Delgado, Y.-L. Lee, S. G. Louie, F. R. Fischer, *Nature* **2021**, *600*, 647–652.
[7] R. Pawlak, X. Liu, S. Ninova, P. D'Astolfo, C. Drechsel, S. Sangtarash, R. Häner, S. Decurtins, H. Sadeghi, C. J. Lambert,

U. Aschauer, S.-X. Liu, E. Meyer, *J. Am. Chem. Soc.* **2020**, *142*, 12568–12573.
[8] Q. Chen, A. Lodi, H. Zhang, A. Gee, H. I. Wang, F. Kong, M. Clarke, M. Edmondson, J. Hart, J. N. O'Shea, W. Stawski, J. Baugh, A. Narita, A. Saywell, M. Bonn, K. Müllen, L. Bogani, H. L. Anderson, *Nat. Chem.* **2024**, *16*, 1133–1140.
[9] Y. Zhong, B. Kumar, S. Oh, M. T. Trinh, Y. Wu, K. Elbert, P. Li, X. Zhu, S. Xiao, F. Ng, M. L. Steigerwald, C. Nuckolls, *J. Am. Chem. Soc.* **2014**, *136*, 8122–8130.
[10] T. J. Sisto, Y. Zhong, B. Zhang, M. T. Trinh, K. Miyata, X. Zhong, X.-Y. Zhu, M. L. Steigerwald, F. Ng, C. Nuckolls, *J. Am. Chem. Soc.* **2017**, *139*, 5648–5651.
[11] X. Wang, J. Ma, W. Zheng, S. Osella, N. Arisnabarreta, J. Droste, G. Serra, O. Ivasenko, A. Lucotti, D. Beljonne, M. Bonn, X. Liu, M. R. Hansen, M. Tommasini, S. De Feyter, J. Liu, H. I. Wang, X. Feng, *J. Am. Chem. Soc.* **2022**, *144*, 228–235.
[12] R. K. Dubey, M. Melle-Franco, A. Mateo-Alonso, *J. Am. Chem. Soc.* **2022**, *144*, 2765–2774.
[13] Z. Jin, Q. Cheng, S. T. Bao, R. Zhang, A. M. Evans, F. Ng, Y. Xu, M. L. Steigerwald, A. E. McDermott, Y. Yang, C. Nuckolls, *J. Am. Chem. Soc.* **2022**, *144*, 13973–13980.
[14] L. Yang, J. Ma, W. Zheng, S. Osella, J. Droste, H. Komber, K. Liu, S. Böckmann, D. Beljonne, M. R. Hansen, M. Bonn, H. I. Wang, J. Liu, X. Feng, *Adv. Sci.* **2022**, *9*, 2200708.
[15] R. K. Dubey, M. Marongiu, S. Fu, G. Wen, M. Bonn, H. I. Wang, M. Melle-Franco, A. Mateo-Alonso, *Chem* **2023**, *9*, 2983–2996.
[16] K. Liu, W. Zheng, S. Osella, Z.-L. Qiu, S. Böckmann, W. Niu, L. Meingast, H. Komber, S. Obermann, R. Gillen, M. Bonn, M. R. Hansen, J. Maultzsch, H. I. Wang, J. Ma, X. Feng, *J. Am. Chem. Soc.* **2024**, *146*, 1026–1034.
[17] P. Izquierdo-García, J. M. Fernández-García, S. M. Rivero, M. Šámal, J. Rybáček, L. Bednárová, S. Ramírez-Barroso, F. J. Ramírez, R. Rodríguez, J. Perles, D. García-Fresnadillo, J. Crassous, J. Casado, I. G. Stará, N. Martín, *J. Am. Chem. Soc.* **2023**, *145*, 11599–11610.
[18] J. Barroso, J. L. Cabellos, S. Pan, F. Murillo, X. Zarate, M. A. Fernandez-Herrera, G. Merino, *Chem. Commun.* **2017**, *54*, 188–191.
[19] S. V. Elshocht, B. Busson, T. Verbiest, M. Kauranen, J. Snauwaert, L. Hellemans, A. Persoons, C. Nuckolls, T. J. Katz, *MRS Online Proc. Libr.* **1999**, *561*, 15.
[20] M. Atzori, K. Dhbaibi, H. Douib, M. Grasser, V. Dorcet, I. Breslavetz, K. Paillot, O. Cador, G. L. J. A. Rikken, B. Le Guennic, J. Crassous, F. Pointillart, C. Train, *J. Am. Chem. Soc.* **2021**, *143*, 2671–2675.
[21] P. Aillard, A. Voituriez, A. Marinetti, *Dalton Trans.* **2014**, *43*, 15263–15278.
[22] R. Naaman, Y. Paltiel, D. H. Waldeck, *Acc. Chem. Res.* **2020**, *53*, 2659–2667.
[23] R. Naaman, Y. Paltiel, D. H. Waldeck, *J. Phys. Chem. Lett.* **2020**, *11*, 3660–3666.
[24] V. Kiran, S. P. Mathew, S. R. Cohen, I. Hernández Delgado, J. Lacour, R. Naaman, *Adv. Mater.* **2016**, *28*, 1957–1962.
[25] S. T. Bao, H. Jiang, C. Schaack, S. Louie, M. L. Steigerwald, C. Nuckolls, Z. Jin, *J. Am. Chem. Soc.* **2022**, *144*, 18772–18777.
[26] S. T. Bao, S. Louie, H. Jiang, Q. Jiang, S. Sun, M. L. Steigerwald, C. Nuckolls, Z. Jin, *J. Am. Chem. Soc.* **2024**, *146*, 51–56.
[27] P. Wang, I. Jeon, Z. Lin, M. D. Peeks, S. Savagatrup, S. E. Kooi, T. Van Voorhis, T. M. Swager, *J. Am. Chem. Soc.* **2018**, *140*, 6501–6508.
[28] C.-K. Lim, M. J. Cho, A. Singh, Q. Li, W. J. Kim, H. S. Jee, K. L. Fillman, S. H. Carpenter, M. L. Neidig, A. Baev, M. T. Swihart, P. N. Prasad, *Nano Lett.* **2016**, *16*, 5451–5455.
[29] A. Satrijo, T. M. Swager, *Macromolecules* **2005**, *38*, 4054–4057.
[30] K. Watanabe, K. Suda, K. Akagi, *J. Mater. Chem. C* **2013**, *1*, 2797.
[31] H. Jiang, D. Čavlović, Q. Jiang, F. Ng, S. T. Bao, E. J. Telford, M. L. Steigerwald, X. Roy, C. Nuckolls, J. M. McNeill, *J. Am. Chem. Soc.* **2025**, *147*, 12982–12988.
[32] K. H. Hendriks, W. Li, G. H. L. Heintges, G. W. P. Van Pruissen, M. M. Wienk, R. A. J. Janssen, *J. Am. Chem. Soc.* **2014**, *136*, 11128–11133.
[33] B. Ma, Q. Shi, X. Ma, Y. Li, H. Chen, K. Wen, R. Zhao, F. Zhang, Y. Lin, Z. Wang, H. Huang, *Angew. Chem. Int. Ed.* **2022**, *61*, e202115969.
[34] K. Ray, S. P. Ananthavel, D. H. Waldeck, R. Naaman, *Science* **1999**, *283*, 814–816.
[35] B. P. Bloom, Y. Paltiel, R. Naaman, D. H. Waldeck, *Chem. Rev.* **2024**, *124*, 1950–1991.
[36] X. Xu, W. Yao, D. Xiao, T. F. Heinz, *Nat. Phys.* **2014**, *10*, 343–350.
[37] S. Shrestha, M. Li, S. Park, X. Tong, D. DiMarzio, M. Cotlet, *Nat. Commun.* **2023**, *14*, 5234.
[38] Y. Chen, J. Ma, Z. Liu, J. Li, X. Duan, D. Li, *ACS Nano* **2020**, *14*, 15154–15160.
[39] C. R. Zhu, K. Zhang, M. Glazov, B. Urbaszek, T. Amand, Z. W. Ji, B. L. Liu, X. Marie, *Phys. Rev. B* **2014**, *90*, 161302.
[40] J. Huang, T. B. Hoang, T. Ming, J. Kong, M. H. Mikkelsen, *Phys. Rev. B* **2017**, *95*, 075428.
[41] F. Liu, W. Wu, Y. Bai, S. H. Chae, Q. Li, J. Wang, J. Hone, X.-Y. Zhu, *Science* **2020**, *367*, 903–906.
[42] E. Sebastian, A. M. Philip, A. Benny, M. Hariharan, *Angew. Chem. Int. Ed.* **2018**, *57*, 15696–15701.
[43] S. Ma, J. Gu, C. Lin, Z. Luo, Y. Zhu, J. Wang, *J. Am. Chem. Soc.* **2020**, *142*, 16887–16893.
[44] B. Mahlmeister, M. Mahl, H. Reichelt, K. Shoyama, M. Stolte, F. Würthner, *J. Am. Chem. Soc.* **2022**, *144*, 10507–10514.
[45] A. Swain, K. Radacki, H. Braunschweig, P. Ravat, *Chem. Sci.* **2024**, *15*, 11737–11747.
[46] S. Sengupta, R. K. Dubey, R. W. M. Hoek, S. P. P. van Eeden, D. D. Gunbaş, F. C. Grozema, E. J. R. Sudhölter, W. F. Jager, *J. Org. Chem.* **2014**, *79*, 6655–6662.
[47] Y. Li, C. Wang, C. Li, S. Di Motta, F. Negri, Z. Wang, *Org. Lett.* **2012**, *14*, 5278–5281.
[48] C. D. Schmidt, N. Lang, N. Jux, A. Hirsch, *Chem. Eur. J.* **2011**, *17*, 5289–5299.
[49] A. D. Bochevarov, E. Harder, T. F. Hughes, J. R. Greenwood, D. A. Braden, D. M. Philipp, D. Rinaldo, M. D. Halls, J. Zhang, R. A. Friesner, *Int. J. Quantum Chem.* **2013**, *113*, 2110–2142.

Manuscript received: April 15, 2025
Revised manuscript received: June 13, 2025
Accepted manuscript online: June 23, 2025
Version of record online: ■■, ■■

Research Article

Graphene Nanoribbons

S. T. Bao, Y. Hong, H. Jiang, L. T. Lackovic, S. Louie, D. Xu, F. Ng, N. Olsen, X. Zhu, M. L. Steigerwald, M. Delor*, C. Nuckolls*, Q. Jiang* —— **e202508426**

Chirality Unbound in Graphene Nanoribbons

This study unveils a method to wind chiral graphene nanoribbons into either right-handed or left-handed helices, depending on the functional groups that adorn their edges. These helically wound graphene nanoribbons act as room-temperature spin filters in thin films due to their chirality-induced spin selectivity.